SURFACE DEFORMATION MONITORING IN SHIYAN BASED ON MULTI-TEMPORAL INSAR TECHNOLOGY

Zilin Zhu[1], Lei Chen[1], Lv Zhou[2*], Yonggui Zhou[1], Zhongliang Zhu[1], Jiahao Li[3], Jiaqi Luo[1], Shenke Xiao[1], Qian Gao[1]

1 PIESAT Information Technology Co., Ltd., BeiJing, China
2 College of Surveying, Mapping and Geographic Information, Guilin University of Technology, Guilin, China
3 Institute of Geospatial Information, Information Engineering University, Zhengzhou, China

KEY WORDS: MT-InSAR, Deformation monitoring, Deformation zones, Spatial and temporal distribution.

ABSTRACT:

In recent years, InSAR technology has continuously developed and become a mainstream technology for monitoring wide-area surface deformation. In this study, Shiyan was selected as the work area, and Multi-temporal Synthetic Aperture Radar Interferometry (MT-InSAR) technology was used to monitor surface deformation over a long time series. The temporal and spatial distribution characteristics of the InSAR monitoring results were analyzed. The surveillance results showed that from January 2021 to March 2023, Shiyan experienced noticeable uneven settlement, with a deformation rate range of [-111.8mm/a, 20.9mm/a]. The maximum cumulative deformation variable reached -212.9mm, and more than 70 deformation zones were identified during the study period. The main causes of deformation were also analyzed. This study provides a reference for large-scale surface deformation monitoring and disaster management in Shiyan.

1. INTRODUCTION

Li (2022) has shown that surface deformation is a geological phenomenon that can be caused by natural or human engineering activities, such as the consolidation and compression of underground loose rock strata, leading to a reduction in surface elevation in a specific area. This slow-forming geological disaster can have devastating effects on buildings, production facilities, urban planning, resource development, and even residents' safety. To mitigate the damage caused by land subsidence, it is crucial to continuously monitor its intensity, rate, and spatial changes. In particular, InSAR technology has proven to be a powerful tool for monitoring land subsidence in large cities and densely populated plain areas. Recent studies including Qu (2019), Chaussard_E (2014), and Bayuaji_L (2010) have demonstrated that rapid urbanization and population growth have increased the demand for water supply in many cities globally. To meet the rising water needs, excessive groundwater extraction coupled with human engineering activities have contributed to land subsidence in various metropolitan areas worldwide, such as Houston, Mexico City, Jakarta, among others. The excessive groundwater pumping leads to the consolidation and compression of underground aquifers and sediments, causing localized surface elevation reduction and geological deformations. These human-induced factors exacerbating land subsidence highlight the urgency of sustainable groundwater management as urban populations continue expanding. Recent studies including Guo (2020), Zhou (2022), Peng 2019), and Liu (2018) have revealed severe land subsidence issues in major Chinese cities such as Beijing, Tianjin, Xi'an, and Taiyuan. The extensive subsidence has posed considerable threats to safety and sustainable development in these urban areas. Therefore, there is an urgent need for large-area, long-term, and high-precision monitoring and research on land subsidence across China. The excessive groundwater extraction and infrastructure projects in these cities have led to the compression of underground sediments and aquifers. This human-induced subsidence highlights the importance of sustainable groundwater management and urban planning to mitigate geological hazards as populations expand.

Recent studies including Zebker_H (1986), Gabriel_A (1989), Hanssen_R (2001), Li (2022), Liao (2022), and Xu (2022) have demonstrated that Interferometric Synthetic Aperture Radar (InSAR) technology has emerged as an important tool for surface topography inversion, owing to its abilities to operate in all weather conditions and achieve high spatio-temporal resolution. Building upon InSAR, Differential InSAR (DInSAR) technology has significantly advanced surface deformation mapping by processing two SAR images with different phases. DInSAR has proven highly effective in applications like co-seismic displacement extraction, landslide monitoring, and geological hazard assessment. However, long temporal differences between SAR image pairs can lead to loss of coherence and measurement errors. Zhu (2017) proposed multi-temporal InSAR techniques to mitigate the issue of loss of coherence and measurement errors caused by long temporal differences between SAR image pairs. By integrating multi-scene SAR data, multi-temporal InSAR can reduce decorrelation effects and enhance deformation monitoring capabilities. The development of InSAR methods highlights their value for studying various surface processes and geohazards. Continued improvements in temporal decorrelation and inversion algorithms can further strengthen InSAR applications. By arranging multi-scene SAR images over a study period according to time series, MT-InSAR technology interferes with each scene image and multiple different SAR images within a certain spatio-temporal range simultaneously, generating multiple interference pairs and reducing the impact of incoherence on measurement results. Furthermore, multi-temporal InSAR is widely used to obtain large-scale surface temporal deformation, thanks to its advantages in multi-scene temporal image processing, which can effectively detect small surface deformation over time.

---

* Corresponding author: zhoulv@glut.edu.cn

2. STUDY AREA AND DATA SOURCE OVERVIEW

2.1 Study area overview

Shiyan is located at the southern foot of Qinba Mountain in the west of Hubei Province, China. Its geographical location is 32°37'-33°50' north latitude and 110°55'-111°38' east longitude. The territory is dominated by mountainous terrain, high in the east and low in the west. With complex geological conditions and special climatic conditions, geological disasters occur frequently. 98.7% of the city's geographical area belongs to the area prone to geological disasters, making it one of the areas prone to geological disasters in the whole province and even the whole country. The stratigraphic lithology in Shiyan is mainly metamorphic rock and sedimentary rock. The metamorphic rock mainly includes gneiss, mica schist, quartzite, quartz sandstone and so on, while the sedimentary rock mainly includes gravel, sandstone, mudstone and so on. There are many ore mining projects on the ground, resulting in the gradual expansion of the scope and trend of land subsidence. The stratigraphic lithology in Shiyan is mainly metamorphic rock and sedimentary rock. The metamorphic rock mainly includes gneiss, mica schist, quartzite, quartz sandstone and so on, while the sedimentary rock mainly includes gravel, sandstone, mudstone and so on. There are many ore mining projects on the ground, resulting in the gradual expansion of the scope and trend of land subsidence. Geographical location in the study area is shown in Figure 1.
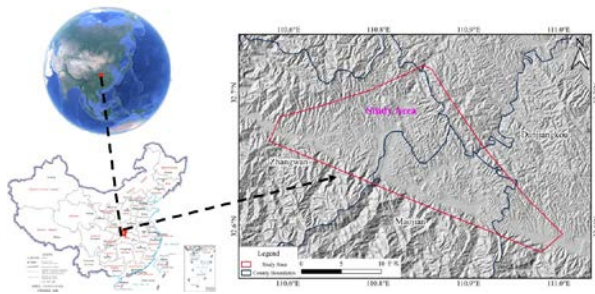

Figure 1. Geographical location of the study area.

In this study, the Sentinel-1A satellite SAR image(https://scihub.copernicus.eu/dhus/#/home) data of 51 Ascent orbit covering Shiyan urban area was adopted. Since 2014, SAR image data acquired by Sentinel-1A has been widely used by scholars around the world in settlement monitoring, hidden danger identification, and emergency monitoring, and has become one of the mainstream SAR satellites in the world. The Sentinel-1A SAR images used in this study to acquire surface subsidence information span from January 2021 to March 2023. The polarization mode is VV polarization, and the range-direction × azimuth-direction resolution is 5 m×20 m, the basic parameters of Sentinel-1A image are showed in Table 1. The digital altitude data is AlOS-12.5m altitude data collected by the phased formation L-band Synthetic aperture radar (PALSAR) of the ALOS (Advanced Land Observing Satellite) satellite launched by the Japan Aerospace Exploration Agency in 2006. In addition, in the process of processing, the precision orbit data(https://scihub.copernicus.eu/gnss/#/home) released by ESA is adopted in this paper for orbit refinement and phase reflattening.

SAR Data	Value
Satellite	Sentinel-1A
Imaging mode	IW
Data type	SLC
Band	C(5.6cm)
Revisit cycle	12 days
Polarization	VV
Time span	January 2021 to March 2023
Orbit	Ascending
Central incidence Angle	37.2°

Table 1. Basic Parameters of Sentinel-1A Image.

3. RESEARCH METHODS

3.1 Principles of MT-InSAR technology

Berardino_P (2002) proposed the MT-InSAR technology that was used in this study to monitor deformation. This technique composes all the SAR images covering the same area into several subsets. The baseline distance of images in subsets (including time baseline distance and space baseline distance) is small, while the baseline distance between subsets is large. After such a simple and effective merger to get all of the available small baseline interference figure. This combination is based on the minimum deformation rate standard, using the singular value decomposition (SVD) method is easy to obtain the minimum deformation rate. The SBAS-InSAR method limits the geometric decoherence caused by the long baseline, and allows more SAR images to participate in the deformation calculation, increasing the sampling in time. In order to solve the large-scale deformation phenomenon under low resolution, the SBAS method is proposed to analyze the surface deformation based on the unwrapped phase image of the subsequent phase unwrapping operation such as the multi-look differential interferogram set, so as to reduce the influence of time and space decorrelation factors and obtain the average deformation speed of the monitoring area.

Assuming there are $M(M>2)$ scene SAR images, according to imaging time order, Assume that the cumulative deformation phase of $(i=0,1,\cdots,M-1)$ the same resolution element (x,r) at the imaging time i is $\varphi(t_i,x,r)$. If the critical baseline condition is satisfied, there are N different interference image pairs, and N differential interference pattern can be generated:

$$\frac{M}{2} \le N \le \frac{M(M-1)}{2} \qquad (1)$$

The deformation phase corresponding to each resolution unit of an interference pattern can be represented by the cumulative deformation phase of the primary and secondary images generating the interference pattern in the observation sequence, namely:

$$\delta\phi_{def}(t_p,x,r) = \phi(t_i,x,r) - \phi(t_j,x,r)$$
$$p = 0,1,\cdots,N-1 \qquad (2)$$

Then the relationship between cumulative deformation phase and interference phase sequence is:

$$A\phi = \delta\phi_{def} \qquad (3)$$

Let's: $\delta\varphi_{def}(\Delta t_0) = \varphi(t_2) - \varphi(t_0)$ $\delta\varphi_{def}(\Delta t_1) = \varphi(t_1) - \varphi(t_0)$ available:

$$A = \begin{bmatrix} -1 & 0 & 1 & 0 & \cdots \\ -1 & 1 & 0 & 0 & \cdots \\ \cdots & \cdots & \cdots & \cdots & \cdots \\ \cdots & \cdots & \cdots & \cdots & \cdots \\ \cdots & \cdots & \cdots & \cdots & \cdots \\ \cdots & \cdots & \cdots & \cdots & \cdots \end{bmatrix}_{N\times M} \qquad (4)$$

$$\varphi = \left[\varphi(t_0), \varphi(t_1), \cdots, \varphi(t_{M-1}) \right]_{M \times 1}^{T} \qquad (5)$$

$$\delta\varphi_{def} = \left[\delta\varphi_{def}(\Delta t_0), \delta\varphi_{def}(\Delta t_1), \cdots, \delta\varphi_{def}(\Delta t_{N-1}) \right]_{N \times 1}^{T} \qquad (6)$$

If all SAR images belong to a short baseline set, the deformation phase can be obtained by using least squares:

$$\hat{\varphi} = (A^T A)^{-1} A^T \delta\varphi_{def} \qquad (7)$$

But in practice, this is less likely. For multiple short baseline sets, $A^T A$ is a singular matrix. The singular value decomposition (SVD) method can be used to solve the generalized inverse matrix A^+ of A:

$$A^+ = V S^{-1} U^T \qquad (8)$$

Among them: $S = diag(\sigma_1, \sigma_2, \cdots, \sigma_r)$, U and V are the left and right singular vector matrices of the corresponding matrices, and r is the rank of matrix A. Then the least square phase estimation in the sense of the smallest norm is:

$$\hat{\varphi} = A^+ \delta\varphi_{def} \qquad (9)$$

Assuming that the deformation phase at the initial time is 0, M deformation cumulants can be obtained as follows:

$$\hat{\varphi} = \left[0, \hat{\varphi}(t_1) - \hat{\varphi}(t_0), \cdots, \hat{\varphi}(t_{M-1}) - \hat{\varphi}(t_0) \right] \qquad (10)$$

To convert phase to average phase velocity:

$$v^T = \left[v_1 = \frac{\varphi_2}{t_2 - t_1}, \cdots, v_{M-1} = \frac{\varphi_M - \varphi_{M-1}}{t_M - t_{M-1}} \right] \qquad (11)$$

Instead of the phase in $\hat{\varphi}$, get:

$$\sum (t_{k+1} - t_k) v_k = \delta\varphi(j)$$
$$j = 0, 1, \cdots, N-1 \qquad (12)$$

Thus a new matrix equation is obtained:

$$Dv = \delta\varphi_{def} \qquad (13)$$

D is a $N \times (M-1)$ matrix. For row j, the column between the acquisition times of the primary and secondary images, $D(j,k) = t_k - t_{k-1}$, Other $D(j,k) = 0$, in this case, apply the SVD decomposition to the matrix D, and you get the minimum norm solution of the velocity vector v.

In the case of surface deformation, elevation error, atmospheric influence and loss of correlation, the differential interference phase composition of each coherent point on each differential interferogram can be expressed as follows:

$$\varphi_{diff} = \varphi_{topo\_e} + \varphi_{def} + \varphi_{orb} + \varphi_{atm} + \varphi_{noise} \qquad (14)$$

Here $\varphi_{topo} = -\frac{4\pi B_\perp}{\lambda R \sin\theta} \varepsilon$ is the residual topographic phase caused by inaccurate DEM data adopted, ε is the elevation error; $\varphi_{def} = -\frac{4\pi}{\lambda} v T + \varphi_{mon}$, T is the time base line of the interferogram, and v is the average deformation rate of the terrain in this time period. φ_{orb} is the orbital error phase introduced in the process of removing the flat ground phase under the imprecise orbital parameters; φ_{atm} and φ_{noise} are the phases introduced by atmosphere and noise, respectively.

Based on the composition of differential interference phase, the equation model of deformation rate and elevation error ε is established, namely:

$$Dv + C\varepsilon = \Delta\varphi \qquad (15)$$

Here, $C(N \times 1)$ is the coefficient matrix associated with the spatial baseline, from which the DEM error can be obtained.

In addition, the atmospheric phase and the nonlinear deformation phase can be separated by continuing to filter the residual phase in space and time on the basis of the linear model. By superimposing the nonlinear deformation phase into the linear deformation phase, the total surface deformation phase can be obtained:

$$\phi_{def} = -\frac{4\pi}{\lambda} v T + \phi_{non} \qquad (16)$$

Then, according to $\Delta R_{disp} = -\frac{\lambda}{4\pi} \Delta\phi_{def}$, obtain the final shape variable.

3.2 MT-InSAR data processing method

The multi-temporal InSAR technology adopted in this study reduces the influence of spatiotemporal incoherence on the interferometry results by limiting the length of the spatiotemporal baseline of the SAR image set and forming a small baseline set, its main processing steps are as follows:1) SAR image sequence registration and interference: SAR images are sorted according to time series. In this experiment, 2022-02-26 is selected as the super main image, and other images are registered with the super main image. At the same time, in order to reduce the influence of the loss of coherence, the temporal baseline was limited to 90 days and the spatial baseline was 45% of the maximum baseline that satisfied the interference processing in the experiment. The range-looks and azimuth-looks multi-looking size is 4:1, after intervention treatment received 190 interference is shown in Figure 2;2) Differential interferogram generation and phase unwinding: Using track information and AlOS-12.5m DEM to remove the flat phase and terrain phase after interference, the differential interference phase information is obtained, and the high coherence points are extracted for phase unwinding. In this paper, the phase solution is converted to the phase change rate calculation, and the singular value decomposition method is used to solve the problem. After solving the phase variation of each time series, the phase time series is calculated and recovered;3) Filter processing and residual phase: The linear deformation signal is solved based on polynomial deformation model, and the elevation error is modeled and solved. Then the linear deformation signal and elevation error are subtracted from the differential interference phase, and the noise phase is removed by spatial low-pass filtering, and atmospheric phase is removed by temporal high-pass filtering, and the nonlinear deformation is obtained;4) Deformation inversion and geocoding: The complete deformation time series can be obtained by adding the nonlinear deformation and linear deformation, and the deformation monitoring results are transformed from radar coordinate system to geographic coordinate system by geocoding through ALOS-12.5m DEM.
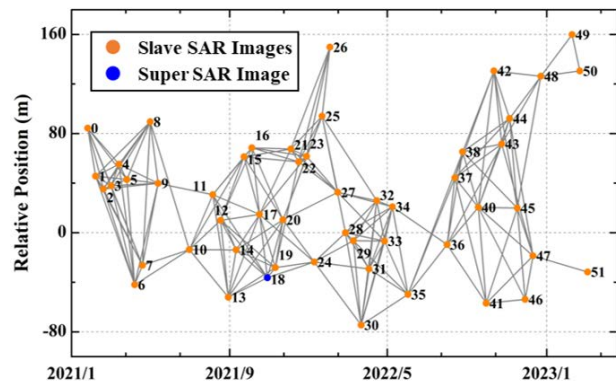

Figure 2. InSAR space-time baseline (orange circles are auxiliary images, blue circles are super main images).

4. TIME SERIES ANALYSIS OF DEFORMATION RESULTS

In this study, the surface deformation information of Shiyan from January 2021 to March 2023 was obtained by MT-InSAR technology. The results show that: During the study period, the deformation rate interval of Shiyan was [-111.8mm/a, 20.9mm/a], and the maximum deformation rate reached -111.8mm/a, with more than 70 obvious deformation clusters. The specific spatial distribution of deformation is shown in Figure 3, where negative values represent downward along the line of sight and positive values represent upward along the line of sight.
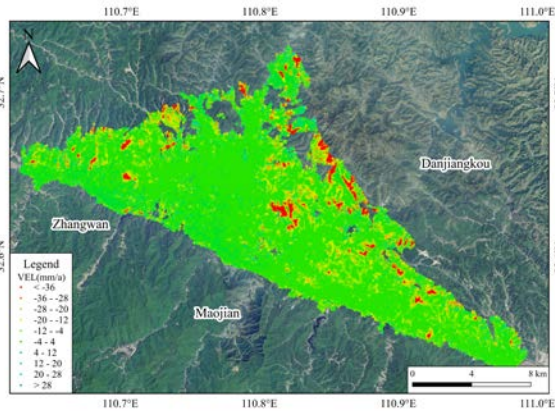

Figure 3. Shiyan city surface deformation rate from January 2021 to March 2023.

In terms of time series, from January 2021 to September 2023, 90% of the Shiyan is basically stable, and the deformation rate interval is [-11.9mm/a, 20.9mm/a]. The study area contains several obvious deformation gathering areas, mainly located in Zhangwan District and Maojian District of Shiyan, and the deformation gathering areas are scattered. Figure 4 shows the temporal changes of cumulative surface deformation in Shiyan during the study period.
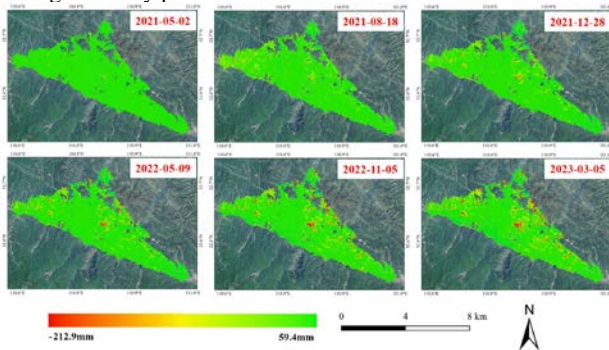

Figure 4. Time series variation of surface deformation in Shiyan from January 2021 to March 2023.

As can be seen from the time series change chart, a small deformation trend has emerged in the central part of Shiyan since May 2021, and the deformation range and shape variable are relatively small. After August 2021, an obvious deformation gathering area has appeared, showing an obvious trend of accelerated expansion. As can be seen from Figure 3 and Figure 4 as a whole, there is an obvious non-uniform settlement phenomenon in Shiyan and an obvious deformation gathering area.

As can be seen from Figure 3, there are obvious deformation gathering areas in Shiyan, and there are certain differences in the area, average deformation rate and cumulative shape variables of each deformation gathering area. In order to more intuitively display the area, deformation rate and cumulative shape variables of each deformation gathering area, the deformation gathering area is delineated as a whole according to a unified deformation rate. Due to the gradual gradient trend in the deformation gathering area, according to the deformation rate of the study area, the boundary of the deformation gathering area was set as the deformation rate less than -20mm/a in this study, and the deformation gathering area was delineated. The distribution of the deformation gathering area is shown in Figure 5. From left to right (top to bottom), they are numbered from 1-70. The basic information of the deformation gathering areas is shown in Table 2. About 32 deformation areas are larger than $0.1km^2$, accounting for 45.7% of the total deformation gathering areas, and the uneven subsidence is relatively obvious.
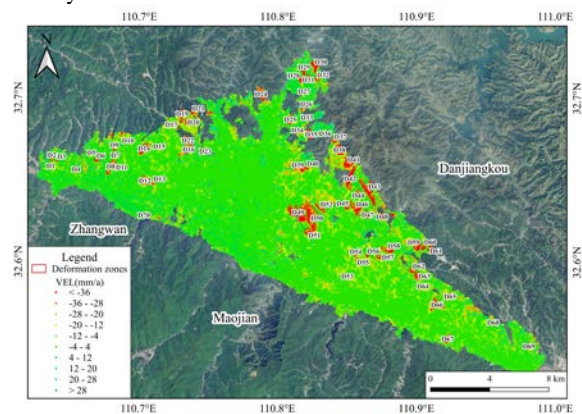

Figure 5. Shiyan surface deformation zones.

NO.	Area (km²)	Central Lon	Central Lat	Max deformation rate(mm/a)	Max cumulative deformation (mm)
D 1	0.07	110.63	32.65	-52.9	-95.4
D 2	0.04	110.63	32.66	-28.1	-51.8
D 3	0.01	110.64	32.66	-24.2	-53.8
D 4	0.03	110.65	32.65	-30.8	-69.6
D 5	0.05	110.66	32.66	-39.1	-78.8
D 6	0.06	110.66	32.66	-50.5	-104.2
D 7	0.04	110.68	32.66	-22.8	-52.3
D 8	0.22	110.68	32.65	-51.1	-109.3
D 9	0.03	110.68	32.66	-26.7	-57.6
D 10	0.03	110.69	32.67	-43.4	-94.1
D 11	0.01	110.68	32.65	-26.8	-55.4
D 12	0.26	110.70	32.64	-65.9	-134.1
D 13	0.04	110.71	32.64	-29.4	-61.1
D 14	0.27	110.70	32.66	-69.3	-148.1
D 15	0.07	110.71	32.67	-22.6	-52.9
D 16	0.19	110.73	32.66	-52.5	-110.5
D 17	0.03	110.72	32.68	-25.4	-52.3
D 18	0.04	110.73	32.68	-46.5	-94.1
D 19	0.06	110.73	32.69	-41.2	-96.6
D 20	0.07	110.73	32.68	-30.5	-63.3
D 21	0.03	110.73	32.69	-50.5	-96.3
D 22	0.14	110.73	32.67	-55.3	-109.5
D 23	0.05	110.74	32.66	-31.4	-70.5
D 24	0.24	110.78	32.70	-61.6	-136.4
D 25	0.12	110.80	32.68	-46.9	-83.4
D 26	0.05	110.82	32.69	-60.7	-117.3
D 27	0.01	110.81	32.70	-32.2	-64.2

D 28	0.10	110.81	32.71	-60.9	-122.8
D 29	0.09	110.81	32.71	-56.6	-115.1
D 30	0.18	110.82	32.72	-111.4	-212.9
D 31	0.03	110.82	32.71	-34.2	-70.9
D 32	0.06	110.82	32.71	-41.9	-90.6
D 33	0.08	110.82	32.68	-43.2	-90.3
D 34	0.05	110.81	32.68	-44.1	-87.4
D 35	0.26	110.82	32.67	-71.7	-138.1
D 36	0.02	110.83	32.67	-43.5	-83.9
D 37	0.05	110.84	32.67	-42.9	-87.2
D 38	0.26	110.84	32.66	-77.3	-170.5
D 39	0.09	110.81	32.65	-49.1	-99.5
D 40	0.04	110.82	32.65	-36.7	-84.1
D 41	0.20	110.85	32.66	-81.9	-146.6
D 42	0.36	110.85	32.65	-68.5	-135.6
D 43	0.53	110.86	32.64	-75.1	-149.8
D 44	0.03	110.85	32.63	-32.1	-62.5
D 45	0.05	110.85	32.6	-48.3	-97.6
D 46	0.28	110.85	32.63	-78.2	-158.4
D 47	0.09	110.86	32.62	-56.4	-118.2
D 48	0.08	110.87	32.62	-88.8	-172.6
D 49	0.72	110.81	32.63	-111.8	-218.4
D 50	0.63	110.82	32.62	-83.7	-161.4
D 51	0.18	110.82	32.61	-64.3	-131.1
D 52	0.11	110.83	32.63	-33.7	-68.3
D 53	0.05	110.8	32.59	-44.4	-85.7
D 54	0.01	110.8	32.60	-27.9	-54.8
D 55	0.02	110.8	32.60	-28.7	-62.9
D 56	0.03	110.8	32.60	-34.7	-68.6
D 57	0.15	110.66	32.60	-72.3	-147.9
D 58	0.16	110.63	32.60	-62.2	-125.3
D 59	0.16	110.64	32.61	-78.6	-154.2
D 60	0.10	110.65	32.61	-90.1	-172.9
D 61	0.06	110.66	32.60	-62.1	-121.2
D 62	0.11	110.66	32.59	-60.5	-119.1
D 63	0.17	110.68	32.59	-68.1	-137.5
D 64	0.05	110.68	32.65	-42.6	-84.8
D 65	0.20	110.68	32.66	-54.6	-107.2
D 66	0.28	110.69	32.66	-55.4	-110.9
D 67	0.14	110.68	32.65	-44.2	-99.8
D 68	0.04	110.70	32.66	-42.6	-84.4
D 69	0.05	110.71	32.66	-39.5	-76.1
D 70	0.12	110.70	32.66	-38.5	-78.6

Table 2. Basic Parameters of deformation zones.

5. SURFACE DEFORMATION CAUSES ANALYSIS

The geological structure of Shiyan working area is very complicated. It is located in the southern belt of East Qinling of the Kunlun and Qinling latitudinal tectonic system, the reflection arc of the west wing of Huaiyangshan zonal tectonic system, the third uplift belt of the New Cathaysian system and the middle part of the second subsidence belt. The regional large faults divide it into different tectonic units, and the control faults are respectively: Qingfeng fault, Zhushan fault and Liangxun fault. Shiyan is very rich in mineral resources. At present, 28 kinds of minerals with pure reserves have been proved. There are 215 mineral producing areas listed in the reserve list of mineral resources in Hubei Province, China, including 15 large deposits (including 2 super-large deposits), 22 medium deposits, 178 small deposits, and more than 600 mineral points. At the same time, Shiyan has many key enterprises. The automobile manufacturing industry, non-ferrous metal smelting industry and metal products industry will have an annual growth in 2022.

It can be seen from the above that the geological environment of the working area of Shiyan is relatively complex, and the large amount of mineral resources mining and the rapid development of manufacturing industry are one of the main reasons for the obvious deformation of Shiyan. In order to find out the cause of deformation and the main time period of deformation, two regions (D12 and D14) with obvious deformation were selected for separate analysis. The deformation rate interval of the deformation zones of D12 is [-65.9mm/a, 9.3mm/a], and the cumulative shape variable interval is [-134.1mm, 19.4mm], and its spatial distribution is shown in Figure 6. As can be seen from Figure 6, there is a large automobile and parts manufacturing plant in the east of the deformation zones of D12. Industrial manufacturing consumes a large amount of groundwater resources, and the mining of surrounding ore resources leads to obvious deformation in this area. In order to understand the time evolution process of deformation more directly, six time series feature points were selected uniformly in the D12 deformation zones to analysis the deformation situation in this area.
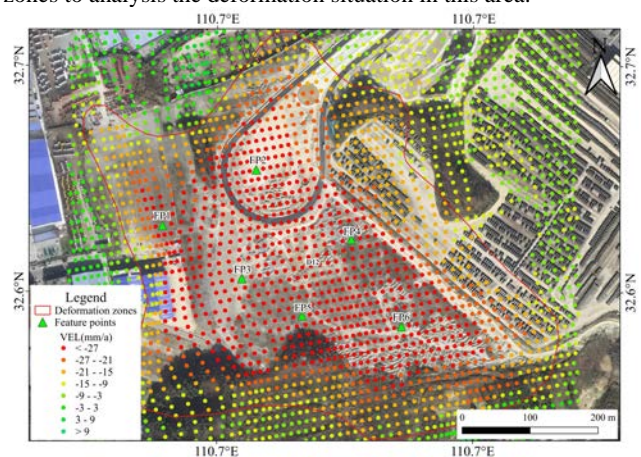

Figure 6. Spatial and temporal distribution of D12 deformation zones.
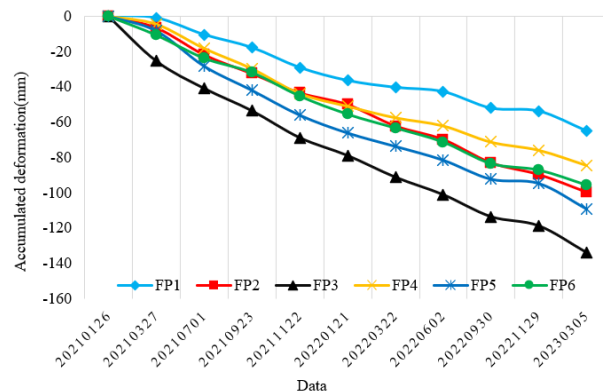

Figure 7. Cumulative shape variables of feature points in D12 deformation zones.

It can be seen from Figure 7 that there is a nonlinear relationship between the cumulative shape variable and time in the D12 deformation agglomeration area. However, with the increase of time, the cumulative shape variable in this area has an increasing trend year by year, and the maximum cumulative shape variable reaches -134.1mm. Among them, the characteristic point of FP3 time series is located in the middle of the region, which increases year by year with the increase of time. Due to the development of large-scale manufacturing industry, a large number of groundwater resources are extracted, and a large number of ore resources are mined, which are the

main reasons for the deformation of the region. At the same time, Shiyan is located in a mid-latitude region with a subtropical monsoon climate, and the rainfall is mainly concentrated from June to September. As can be seen from Figure 7, there is an obvious deformation trend during the period of rainfall. Rainfall supplements the groundwater content, so a relatively gentle deformation trend occurs during September to November. Therefore, rainfall may also be one of the factors affecting surface deformation.

The deformation rate interval of the D14 deformation zones is [-79.9mm/a, 9.4mm/a], and the cumulative shape variable interval is [-170.4mm, 20.1mm], and its spatial distribution is shown in Figure 8. As can be seen from Figure 8, there are obvious working faces left by ore resource mining in this region, so mining of ore is one of the main reasons for ground deformation. In order to understand the time evolution process of deformation more directly, six times sequence feature points were selected uniformly in the D14 deformation zones to analysis the deformation situation in this area.
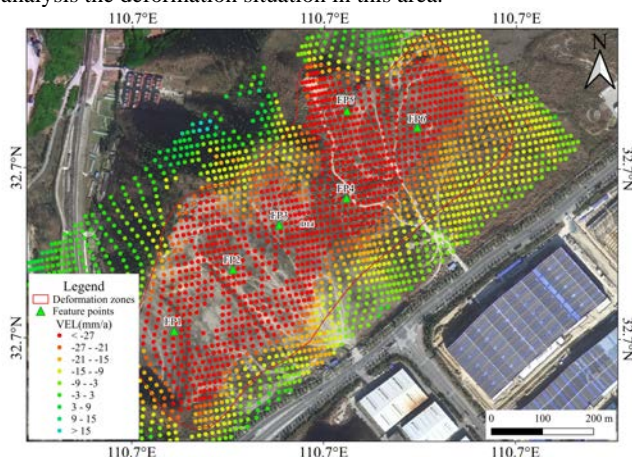

Figure 8. Spatial and temporal distribution of D14 deformation zones.
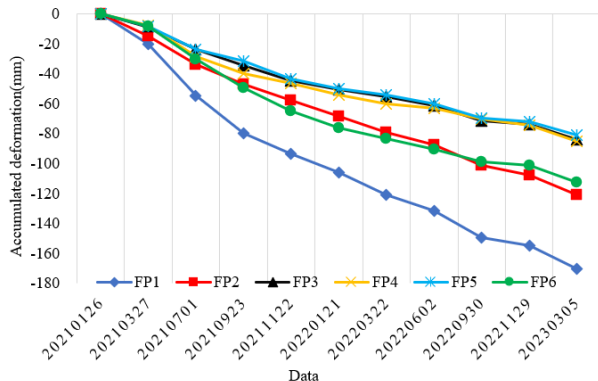

Figure 9. Cumulative shape variables of feature points in D14 deformation zones.

It can be seen from Figure 9 that there is a nonlinear relationship between the cumulative shape variable and time in the D14 deformation agglomeration area. However, with the increase of time, the cumulative shape variable in this area has an increasing trend year by year, and the maximum cumulative shape variable reaches -170.4mm. From the overall results, the cumulative shape variable from March 2021 to September 2021 is large, and the cumulative shape variable reaches -67mm, which may be due to the increase of ore resources mining during March to September, leading to the deformation in this region.

6. CONCLUSION

The multi-temporal InSAR technology and Senitnel-1 data were used to carry out long-term deformation monitoring in Shiyan. The cumulative shape variables and spatial distribution characteristics of the time series of land subsidence in this area from January 2021 to March 2023 were obtained, and the surface deformation rate field in this area was determined. On this basis, about 70 deformation gathering areas were defined. The region of abnormal deformation is determined. Results show that: The maximum deformation rate of surface deformation in Shiyan reached -111.8mm/a, and the maximum cumulative shape variable reached -212.9mm. The deformation trend showed scattered and uneven distribution, and showed an obvious outward expansion trend. Because of the abundant mineral resources in Shiyan, the mining of mineral resources is one of the main reasons for the surface deformation in Shiyan. This study provides a reference for large-scale surface deformation monitoring and disaster management in Shiyan, so as to avoid the destruction of resources and economic losses caused by large-scale geological disasters, and cause more serious waste of resources, so as to achieve sustainable development.

REFERENCES

Li, Z.H., Zhu, W., Yu, C., 2022: Interferometric synthetic aperture radar for deformation mapping: opportunities, challenges and the outlook[J]. Acta Geodaetica et Cartographica Sinica, 51(7):1485-1519.

Qu, F.F., Lu, Z., Kim J. W., 2019: Identify and monitor growth faulting using InSAR over northern Greater Houston, Texas, USA[J]. Remote Sensing, 11(12): 1498

Chaussard, E., Wdowinski, S., Cabral-Cano, E.,2014: Land subsidence in central Mexico detected by ALOS InSAR time-series[J]. Remote Sensing of Environment,140:94-106.

Bayuaji, L., Sumantyo, J.Y.S., Kuze, H., 2010: ALOS PALSAR D-InSAR for land subsidence mapping in Jakarta, Indonesia[J]. Canadian Journal of Remote Sensing,36(1):1-8.

Guo, L., Gong, H.L., Li, J.W.,2020: Understanding uneven land subsidence in Beijing, China, using a novel combination of geophysical prospecting and InSAR[J]. Geophysical Research Letters,47(16).

Zhou, L., ZHAO, Y.Z., Zhu, Z.Z., 2022: Spatialand temporal evolution of surface subsidence in Tianjin from 2015 to 2020 based on SBAS-InSAR technology[J]Journal of Geodesy and Geoinformation Science,5(1): 60-72.

Peng, M.M., Zhao, C.Y., Zhang, Q., 2019: Research on spatiotemporal land deformation (2012--2018) over Xi'an, China, with multi-sensor SAR datasets[J]Remote Sensing, 11(6): 664.

Liu, Y.Y., Zhao, C.Y., Zhang, Q., 2018: Land subsidence in Taiyuan, China, monitored by InSAR technique with multisensor SAR datasets from1992 to 2015[J].IEEE Journal of Selected Topics in Applied Earth Observations and Remote Sensing,11(5): 1509-1519.

Zebker, H.A., Goldstein, R.M.,1986: Topographic mapping from interferometric synthetic aperture radar observations[J]. Journal of Geophysical Research: Solid Earth,91(B5):4993-4999.

Gabriel, A.K., Goldstein, R.M., Zebker, H.A., 1989: Mapping small elevation changes over large areas: differential radar interferometry[J]. Journal of Geophysical Research: Solid Earth, 94(B7):9183-9191.

Hanssen, R.F., 2001, Radar Interferometry: Data Interpretation and Error Analysis[M]. Netherlands: Springer.

Li, Z.H., Han, B.Q., Liu, Z.J., 2022: Source Parameters and Slip Distributions of the 2016 and 2022 Menyuan, Qinghai Earthquakes Constrained by InSAR Observations[J]. Geomatics and Information Science of Wuhan University,47(6):887-897.

Liao, M.S., Dong, J., Li, M.H., 2022: Radar remote sensing for potential landslides detection and deformation monitoring. National Remote Sensing Bulletin,25(1):332-341.

Xu, Q., Cuo, C., Dong, X.J., 2022: Application status and prospect of aerial remote sensing technology for geohazards [J]. Acta Geodaetica et Cartographica Sinica,51(10);2020-2033.

Zhu, J.J., Li, Z.W., Hu, J., 2017: Research Progress and Methods of InSAR for Deformation Monitoring. [J]. Acta Geodaetica et Cartographica Sinica,46(10):1717-1733.

Berardio, P., Fornaro, G., Lanari, R., 2002: A new algorithm for surface deformation monitoring based on small baseline differential SAR interferograms[J]. IEEE Transactions on Geoscience and Remote Sensing, 40(11): 2375-2383.

Hooper, A.J.,2006: Persistent Scatter Radar Interferometry for Crustal Deformation Studies and Modeling of Volcanic Deformation[D]. California: Stanford University.